CrossMark

The novel catalysts of truncated polyhedron Pt nanoparticles supported on three-dimensionally ordered macroporous oxides (Mn, Fe, Co, Ni, Cu) with nanoporous walls for soot combustion

Yuechang Wei, Zhen Zhao*, Teng Li, Jian Liu, Aijun Duan, Guiyuan Jiang

State Key Laboratory of Heavy Oil Processing, Beijing Key Laboratory of Oil and Gas Pollution Control, China University of Petroleum, Beijing 102249, China

ABSTRACT

Three-dimensionally ordered macroporous (3DOM) transition metal oxides (TMO) (Mn, Fe, Co, Ni, Cu) with nanoporous walls were synthesized by the surfactant (P123)-assisted colloidal crystal template (CCT) method, and 3DOM TMO-supported truncated polyhedron Pt nanoparticle catalysts were prepared by the gas bubbling-assisted membrane reduction (GBMR) method. All the catalysts possessed well-defined 3DOM nanostructure with small interconnected pore windows (∼80 nm). The nanopores with the size of ∼6 nm and truncated polyhedron Pt nanoparticles with the sizes of 2.9–3.5 nm are highly dispersed on the inner walls of uniform macropores. 3DOM Pt/TMO catalysts with nanoporous walls exhibit the large total pore volume (∼3.4 ml g^{-1}), the high porosity (>91%) and surface area (36–40 m^2 g^{-1}). 3DOM structure improves the contact efficiency between catalyst and soot, and the strong metal (Pt)–support (TMO) interaction is favorable for the improvement of reducibility and for increasing the amount of active oxygen species. Among all of 3DOM Pt/TMO catalysts with nanoporous walls, Fe- and Co-based catalysts with the moderate reducibility exhibited higher catalytic activity for diesel soot combustion in contrast to the others. For instance, the T_{50} of 3DOM Pt/Fe$_2$O$_3$ and Pt/Co$_3$O$_4$ catalysts are 358 and 351 °C, respectively. And the nanopores on the inner walls of 3DOM Pt/TMO catalysts remarkably improve the S$_{CO2}$ for soot oxidation, and it is nearly 100% in a wide temperature range (200–450 °C). The excellent performance of the catalysts for soot combustion might be due to the factors including unique 3DOM structure with nanoporous walls, highly active component (Pt), large surface area, and the moderate reducibility of the materials. The materials consist of 3DOM supports with nanoporous walls and metal nanoparticle active sites may be the potential practical applications in the catalytic oxidation of diesel soot particles.

© 2013 Elsevier B.V. All rights reserved.

1. Introduction

Soot particles emitted from diesel engines as a typical particulate matter (PM) can cause acute human health and environmental problems [1]. This calls for efficient treatment systems for the exhaust gas from diesel engines [2]. The combination of traps and oxidation catalysts in the continuously regenerating particulate trap (CRT) appears to be one efficient after-treatment technique for diesel engines [3,4]. The key challenge is to find effective catalysts for soot combustion that operates at low temperatures. Noble metals [5,6], transition metal oxides [7,8], alkaline metal oxides [9,10], perovskite-like type oxides [11,12] and rare earth oxides [13,14] have exhibited good catalytic performances for diesel soot combustion. In particular, transition metal oxides (Mn, Fe, Co, Ni,

Cu) are one of the key components in auto-exhaust treatment catalysts [7,8,13]. To design and synthesize high-performance materials in terms of catalytic activity, understanding the properties affecting catalytic performance is of great importance. The catalytic performance for soot combustion is affected by two factors: the contact between soot particles and the catalyst, and the intrinsic activity of the catalyst [4,10,15]. For conventional catalysts with smaller pore sizes (<10 nm) or no pore, it is difficult for soot particles (>25 nm) to enter the inner pores of these catalysts with high surface area, and only those in external surfaces of catalysts are available for soot combustion. Thus, the catalytic activity for soot combustion may be restricted by the poor soot/catalyst contact and/or limited active sites. One way to increase the contact between solid reactant and catalyst is through fabricating macroporous nanostructure materials [16].

Three-dimensionally ordered macroporous (3DOM) metal oxides with uniform pore size (>50 nm) and well-defined structure have drawn much attention in the field of heterogeneous catalysis [17]. The macroporous structures could not only permit soot

* Corresponding author at: 18# Fuxue Road, Chang Ping District, Beijing, 102249, China. Tel.: +86 10 89731586; fax: +86 10 69724721.
E-mail address: zhenzhao@cup.edu.cn (Z. Zhao).

particles to enter their inner pores, but also could allow the soot particles easily transfer through the structure and less diffusion resistance to access the active sites. Thus, the contact between soot and catalyst will be improved remarkably, and 3DOM metal oxides exhibited better catalytic performance for diesel soot oxidation in comparison with disordered macroporous and nanoparticles samples [18,19]. However, their catalytic performances are also limited by their intrinsic activity, i.e., the catalytic combustion of diesel soot particles occur at higher temperatures (ca. 350–500 °C) than the exhaust gas temperatures (ca. 150–400 °C) [1–14]. In the mechanism of catalytic combustion for diesel soot particles, the reaction pathways for catalyzing soot combustion can be divided into two parts: one is that active oxygen species over the surface of the catalysts directly oxidize soot particles; the other one is that NO_x acts as an intermediate to facilitate the indirect catalytic soot oxidation [20]. Therefore, it is also important to improve the intrinsic activity of 3DOM oxide-based catalysts, i.e., enhanced the activation capability of the catalysts for gas reactant (O_2 and NO).

Noble metal nanoparticles are possible choices for enhancing the intrinsic catalytic activity of 3DOM metal oxides [21,22]. The origins of the noble metal-supports synergistic effect have been proposed in the catalysis literature [23–25]. In our previous works, 3DOM oxides-supported gold (Au) catalysts exhibited high catalytic activities for soot combustion, but their thermal stabilities are poor [26,27]. Oxides-supported platinum (Pt) catalysts are still the best catalysts in the literature and also the only commercial catalysts for soot combustion [5,6,28]. The catalytic performance of Pt nanocrystals can be finely tuned by their shape and the strong metal-support interactions (SMSI), which determines surface atomic arrangement and coordination [29]. Nevertheless, all of the mentioned 3DOM transition metal oxides possessed low surface areas due to no mesopores or nanovoids on the walls, leading to the lower adsorption and activation capability for O_2 and NO. In recent years, 3DOM oxides with mesoporous or nanoporous walls have been synthesized and exhibited super catalytic performance for the volatile compounds oxidation and formaldehyde [16,30,31]. However, the preparation and catalytic application of 3DOM metal oxides with mesoporous or nanoporous walls for catalytic soot oxidation have not been reported in the literature. Moreover, the catalysts of truncated polyhedron Pt nanoparticles bounded by high-index facets over 3DOM transition metal oxide with nanoporous walls are potential route to enhance their catalytic activities for soot oxidation.

In the present work, a series of 3DOM transition metal oxides (TMO: Mn, Fe, Co, Ni, Cu) with nanoporous walls were synthesized by the colloidal crystal template (CCT) method. During the preparation process, a surfactant (P123) was introduced into the metal precursor solution for the generation of mesoporous or nanoporous walls, which is beneficial for the improvement of physicochemical property. And 3DOM TMO-supported truncated polyhedron Pt catalysts were designed and synthesized by the gas bubbling-assisted membrane reduction (GBMR) method using poly (N-vinyl-2-pyrrolidone) (PVP) as a stabilizer [20]. The novel catalysts of truncated polyhedron Pt nanoparticles supported on 3DOM TMO with nanoporous walls exhibited high catalytic activity for soot combustion. The composition and structure effects of 3DOM TMO with nanoporous walls on the catalytic activity of 3DOM Pt_n/TMO catalysts for soot combustion were systematically investigated.

2. Experimental

2.1. Catalyst preparation

Schematic representation of the preparation processing of 3DOM TMO with nanoporous walls supported truncated polyhedron Pt nanoparticles catalysts is shown in Fig. 1, and the synthetic method involving two processes is presented in detail as follows.

2.1.1. Preparation of 3DOM TMO (M: Mn, Fe, Co, Ni, Cu) with nanoporous walls

Syntheses of monodispersed polymethyl methacrylate (PMMA) microsphere with an average diameter of ca. 350 nm, and assembly of colloidal crystal template (CCT) by centrifuge method with 3000 rpt min^{-1} for 10 h, were described elsewhere in detail [20]. The obtained CCT was dried at the room temperature and saved in the drying oven at 50 °C. 3DOM TMO (M: Mn, Fe, Co, Ni, Cu) with nanoporous walls supports were prepared using the surfactant-assisted CCT method. In a typical process, the P123 surfactant (2 g) with an average molecular weight of 5800 g mol^{-1} and the citric acid (5 g) as complexing agent were added to the ethylene glycol and methanol (30 vol%) solution (50 ml) that was stirred for 1 h to get a uniform precursor solution. Then the suitable amounts of each metal nitrates ($Mn(NO_3)_2$, $Fe(NO_3)_3 \cdot 9H_2O$, $Co(NO_3)_2 \cdot 6H_2O$, $Ni(NO_3)_2 \cdot 6H_2O$, $Cu(NO_3)_2 \cdot 3H_2O$) was dissolved to obtain transparent solution under stirring at 35 °C for 4 h and the total metal concentration for each solution was 2 mol L^{-1}. The PMMA hard template was soaked in the obtained mixed solution for 4 h. Excess solution was removed from the impregnated templates by filtration. The obtained precursor/template mixture was dried in air at 50 °C for 24 h. And then the dried sample mixed with quartz sand (10–15 meshes) was calcined to remove the PMMA hard template and the P123 soft template in a tube furnace. The thermal treatment process was divided into two steps: (i) the dried solid was calcined in a Ar flow of 80 ml min^{-1} at a ramp of 1 °C min^{-1} from 30 to 310 °C and kept at this temperature for 3 h; and (ii) the treated solid was kept at 310 °C for 1 h in an air flow of 80 ml min^{-1}, then it was heated from 310 to 550 °C in the air at a ramp of 1 °C min^{-1} and held at 550 °C for 4 h. Finally, 3DOM TMO (M: MnO_2, Fe_2O_3, Co_3O_4, NiO, CuO) supports with nanoporous walls were thus obtained. For comparison, 3DOM TMO supports without nanoporous walls were also prepared by the CCT method without soft template (P123). All of the chemicals (A.R. in purity) were purchased from Beijing Chemical Company and used without further purification.

2.1.2. Preparation of 3DOM Pt/TMO catalysts with nanoporous walls

The synthesis of 3DOM Pt/TMO catalysts was carried out by GBMR method which was just developed in our lab [20,26,27]. The detailed synthesis mechanism of 3DOM TMO with nanoporous walls supported Pt nanoparticle catalysts is shown in Supplementary Material, and the schematic diagrams of the GBMR method
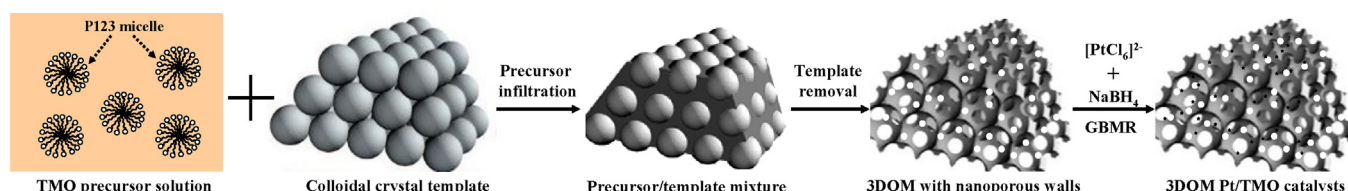

Fig. 1. Schematic representation of the preparation processing of 3DOM TMO with nanoporous walls-supported Pt nanoparticles catalysts.

are illustrated in Figs. S1 and S2. The typical preparation procedure is described as follows: the poly (N-vinyl-2-pyrrolidone) (PVP) solution as a stabilizer was added into H_2PtCl_6 solution, and the $[PVP_{unit}]/[Pt]$ molar ratio is 100. Then 3DOM TMO with nanoporous walls (0.5 g) were also added into the above mentioned solution (50 ml). The mixture solution was driven by a peristaltic pump (Baoding Lange Co., Ltd., China) with rotation speed of 200 rpm ($\sim$360 ml min^{-1}) to form a tubal cycling flow. A reductant solution (NaBH$_4$) (1 ml min^{-1}, 50 ml) was injected into the membrane reactor via the abundant holes (d = 40 nm) on the walls of the two ceramic membrane tubes (Ø 3 mm × 160 mm, Hyflux Group of Companies, Singapore) by a constant flow pump (HLB-2020, Satellite Manufactory of Beijing), and the molar ratio of [NaBH$_4$]/[Pt] is 5. In the meantime, the hydrogen gas was introduced into the membrane reactor via the other two ceramic membrane tubes. The reduction of metal ions occurred immediately when the metal precursor solution flowed into the glass tube reactor. The hydrogen bubbling-assisted stirring operation (40 ml min^{-1}) was developed to vigorously stir the solution. The synthesis process did not stop until complete consumption of the NaBH$_4$ solution. The reaction system was further vigorously bubbled with hydrogen gas for 1 h. Then, the mixture was filtered and washed with distilled water at 60 °C until the Cl$^-$ was completely removed, which was detected by AgNO$_3$. And the final product was calcined in a muffle furnace at 550 °C for 1 h in static air. Finally, the desired 3DOM TMO with nanoporous walls supported truncated polyhedron Pt nanoparticles catalysts were obtained. 3DOM Pt/TMO catalysts with nanoporous walls will be generically named as 3DOM Pt/TMO catalysts, where the nominal weight percent of platinum in catalysts is 2 wt%. For comparison, 3DOM TMO without nanoporous walls supported Pt nanoparticles catalysts named as 3DOM Pt/TMO-NNP catalyst were also prepared by the GBMR method.

2.2. Characterization techniques

The nitrogen adsorption/desorption isotherm was obtained at −196 °C by using an automated gas sorption analyzer (Quantachrome Autosorb-iQ, USA) after having degassed the sample for 4 h at 300 °C. The specific area was calculated from the Brunauer–Emmett–Teller (BET) equation using p/p_0 values between 0.05 and 0.3, and the pore-size distribution was obtained from the desorption branch using the BJH method. Mercury intrusion porosimetry (MIP) experiments were carried out on a Micromeritics AutoPoreIV 9500 apparatus in the pressure range of 0–30,000 psia. X-ray diffraction (XRD) patterns were measured on a powder X-ray diffractometer (Shimadzu XRD 6000) using Cu Kα (λ = 0.15406 nm) radiation with a Nickel filter operating at 40 kV and 10 mA in the 2θ range of 20–80° at a scanning rate of 4° min^{-1}. The patterns were compared with JCPDS reference data for phase identification. The crystallite sizes of obtained samples were calculated from the width of the (1 1 1) peak using the Scherrer equation: $D = 0.9\lambda/(\beta \cos\theta)$, where λ is the wavelength of the radiation, β is the corrected peak width at half-maximum intensity (FWHM), and θ is the peak position. The actual content of Pt in catalysts was determined by inductive coupled plasma atomic emission spectrometry (ICP-AES) (PerkinElmer, Optima 5300DV). The field emission scanning electron microscopy (FESEM) images were observed on a Quanta 200F instrument using accelerating voltages of 5 kV. The transmission electron microscope (TEM) and high-resolution transmission electron microscope (HRTEM) images were obtained using a JEOl JEM 2100 electron microscope at an accelerating voltage of 200 kV. The average particle diameter (d) was calculated by the following formula: $d = \sum n_i d_i / \sum n_i$, where n_i is the number of particle diameter d_i in a certain range, and $\sum n_i$ is more than 300 Pt particles on TEM images of the sample. X-ray

photoelectron spectra (XPS) were recorded on a PerkinElmer PHI-1600 ESCA spectrometer using Mg Kα X-ray source. The binding energies were calibrated using C1s peak of contaminant carbon (BE = 284.38 eV) as an internal standard.

Temperature-programmed reduction with H_2 (H_2-TPR) measurements was performed in a conventional flow apparatus. 100 mg sample was pretreated in an Ar atmosphere at 200 °C for 1 h and subsequently cooled to 30 °C. Then 10% H_2/Ar flow (40 ml min^{-1}) was passed through the catalyst bed while the temperature was ramped up from 30 to 900 °C at a heating rate of 10 °C min^{-1}. The hydrogen consumption signal was monitored by a thermal conductivity detector (TCD). Before the outlet gases entering the TCD, a cooling trap and a filter packed with 5A molecular sieve (60–80 meshes) were used to remove H_2O and CO_2. The temperature-programmed oxidation (TPO) of NO experiment was performed on the above fixed beds for studying the formation of NO_2. Reactant gas compositions were 5% O_2 and 0.2% NO with He balanced gas. The reaction temperature ranged from 100 to 500 °C. The weight of catalyst was 100 mg and no soot was used during the reaction. The other reaction conditions were the same as the following TPO experiment. The NO_2 concentration in the outlet gas was in situ detected by the Quantachrome Autosorb-1 C (USA) combined with a Mass Spectrometer (OminStar^{TM} GSD 301 O2, Balzers) detection.

2.3. Activity tests

The catalytic activities of all catalysts were evaluated with a TPO reaction on a fixed-bed tubular quartz system (ϕ = 8 mm) from 150 to 650 °C at a heating rate of 2 °C min^{-1}. The model soot was Printex-U (diameter $\sim$25 nm, purchased from Degussa). Elemental analysis of Printex-U particulates showed its carbonaceous nature with 92.0% C, 0.7% H, 3.5% O, 0.1% N, 0.2% S and 3.5% other [32]. The catalyst (100 mg) and soot (10 mg) were mixed at a weight ratio of 10:1 with a spatula in order to reproduce the loose contact mode. Reactant gases (50 ml min^{-1}) contain 5% O_2 and 0.2% NO balanced with Ar, or 5% O_2 balanced with Ar. The outlet gas compositions were analyzed by an on-line gas chromatograph (GC, Sp-3420, Beijing) with a flame ionization detector (FID). The catalytic activity was evaluated by the values of T_{10}, T_{50}, and T_{90}, which were defined as the temperatures at 10, 50 and 90% of soot conversion, respectively. The selectivity to CO_2 formation (S_{CO_2}) was defined as that the CO_2 concentration (C_{CO_2}) divided by the sum of the CO_2 and CO concentration, i.e., $S_{CO_2} = C_{CO_2}/(C_{CO} + C_{CO_2})$. $S_{CO_2}^m$ was denoted as S_{CO_2} at which the C_{CO_2} was the maximum. In all TPO experiments, the reactions were not finished until the soot was completely burnt off.

3. Results

3.1. The results of XRD characterization

To confirm the formation and phase structures of 3DOM TMO and Pt/TMO catalysts (M: Mn, Fe, Co, Ni, Cu), XRD measurements were carried out, and the results are shown in Fig. 2. By referring to the XRD pattern of standard TMO samples, all the diffraction peaks of 3DOM TMO and Pt/MTO catalysts correspond to a cubic structure of Mn_2O_3 (JCPDS PDF# 41-1442), a rhombohedral structure of Fe_2O_3 (JCPDS PDF# 33-0664), a cubic structure of Co_3O_4 (JCPDS PDF# 78-1970), a cubic structure of NiO (JCPDS PDF# 71-1179) and a monoclinic structure of CuO (JCPDS PDF# 80-0076), respectively. The Bragg diffraction peaks of all TMO catalysts in the 2θ range of 20–85° could be indexed, as indicated in Fig. 2. It is observed that there was no significant difference in peak types, and the single symmetric diffraction peaks were observed, indicating that all of

Table 1
Average crystal parameters and crystal sizes of the 3DOM TMO and Pt/TMO catalysts with nanoporous walls.

3DOM catalysts	D[a]/nm (support)	Crystal phases	Pt size[b]/nm	Pt content[c] (wt%)
Pt/Mn$_2$O$_3$(Mn$_2$O$_3$)	28 (28)	Cubic	3.3	1.6
Pt/Fe$_2$O$_3$(Fe$_2$O$_3$)	36 (35)	Rhombohedral	2.9	1.7
Pt/Co$_3$O$_4$(Co$_3$O$_4$)	41 (40)	Cubic	3.1	1.7
Pt/NiO(NiO)	27 (27)	Cubic	3.5	1.6
Pt/CuO(CuO)	26 (26)	Monoclinic	3.4	1.5

[a] Determined by XRD using Scherrer equation with the most prominent peak of TMO supports.
[b] Determined by HRTEM.
[c] Determined by inductive coupled plasma atomic emission spectrometry.

the as-prepared catalysts possess the single-phase crystal structure. The XRD patterns of 3DOM TMO and Pt/TMO catalysts display high diffraction feature, implying the good crystallite structure of TMO support. The characteristic diffraction peak ($\sim$39.7°) belonging to the (1 1 1) crystal plane of the face-centered-cubic phase Pt nanoparticles is not detected except for Pt/NiO catalyst due to the detection limitation of XRD measurements, indicating the high dispersion and small size of Pt particles on the surface of 3DOM TMO supports. The average crystallite sizes (D) of all catalysts are estimated by the Debye-Scherrer equation using the XRD data of the most prominent line: $D(h\,k\,l) = 0.89\lambda/(\beta\cos\theta)$, where β is the half-height width of the diffraction peak of catalyst, θ is the diffraction angle, and λ is the X-ray wavelength corresponding to the Cu Kα radiation. The average crystallite sizes of 3DOM TMO supports in the catalysts are about $\sim$28 nm (Mn$_2$O$_3$), $\sim$36 nm (Fe$_2$O$_3$), $\sim$48 nm (Co$_3$O$_4$), $\sim$27 nm (NiO), and $\sim$26 nm (CuO), as listed in Table 1, which corresponds to ca. 1–2 crystalline grains per 3DOM TMO

wall thickness. And the crystallite sizes of 3DOM TMO supports have no apparent change after the deposition of Pt nanoparticles. Therefore, it can be concluded that the deposition of Pt nanoparticles on the surface of 3DOM TMO supports leads to less impact on the crystalline phase, crystalline size, and crystallinity of 3DOM TMO supports.

3.2. The results of SEM characterization

The morphology and macroporous structure of all samples were investigated by means of FESEM technique. Highly ordered macroporous structures could be obtained via the long-range replication of the three-dimensionally close-packed PMMA template. In the preparation process, the component of precursor solution containing the transition metal (M: Mn, Fe, Co, Ni, Cu) nitrates and the hard and soft polymer templates are very important for obtaining high-quality 3DOM TMO with nanoporous walls. Because solidification by nitrate decomposition and melting of the PMMA would occur at the same time, and some of the metal salts were squeezed out from the voids in the template and thus causing low fraction of 3DOM structure. Therefore, the citric acid as complexing agent was added to the precursor solution. The interaction of the citric acid and metal nitrates would produce solid metal-citric acid complexes [33] before the melting of the PMMA template, and hence generating the desired 3DOM complex metal oxide intermediates. Fig. 3 shows SEM images of 3DOM TMO support obtained by the surfactant (P123)-assisted CCT method and 3DOM Pt/MTO catalysts (M: Mn, Fe, Co, Ni, Cu) obtained by GBMR method. For comparison, SEM images of 3DOM Pt/TMO catalysts without nanoporous walls prepared by the CCT method without soft template (P123) are shown in Fig. S3. The macroporous materials contain a skeleton surrounding uniform close-packed periodic voids with the average diameter of 260 ± 10 nm, which corresponds to shrinkage of 25–30% compared with the initial size (350 nm) of PMMA microspheres [26]. This shrinkage is caused by the melting of polymer templates and the sintering of the produced metal oxides. In addition, the wall thicknesses observed from SEM images are 35 ± 5 nm. The next layer is highly visible and the voids are interconnected through the open window, ca. 80 ± 5 nm in diameter. 3DOM Pt/TMO catalysts are similar to the well-defined 3DOM TMO support. It indicates that the synthesis process of GBMR method rarely destroys 3DOM structure.

3.3. The results of MIP and BET characterizations

The presence of macropore in 3DOM catalysts was further assessed by means of MIP. Fig. 4(A) displays the differential curves of pore size distribution of 3DOM Pt/TMO catalysts (M: Mn, Fe, Co, Ni, Cu) as representative examples. The diameter corresponding to the peak value of the different curve is regarded as the most probable pore diameter. The narrower the most probable pore diameter is, the finer the pore structure is. The macropores (50–200 nm) in these samples are very regular, and the most probable pore diameters of all catalysts are in the range of 76.0–78.5 nm, which are
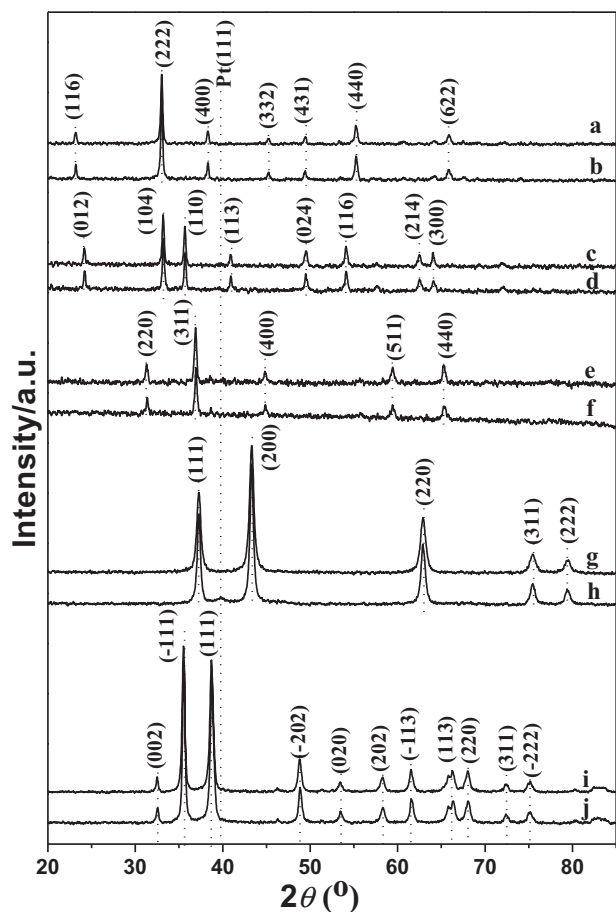

Fig. 2. XRD patterns of 3DOM TMO and Pt/TMO catalysts. a. Mn$_2$O$_3$; b. Pt/Mn$_2$O$_3$; c.Fe$_2$O$_3$; d. Pt/Fe$_2$O$_3$; e. Co$_3$O$_4$; f. Pt/Co$_3$O$_4$; g. NiO; h. Pt/NiO; i. CuO; j. Pt/CuO.
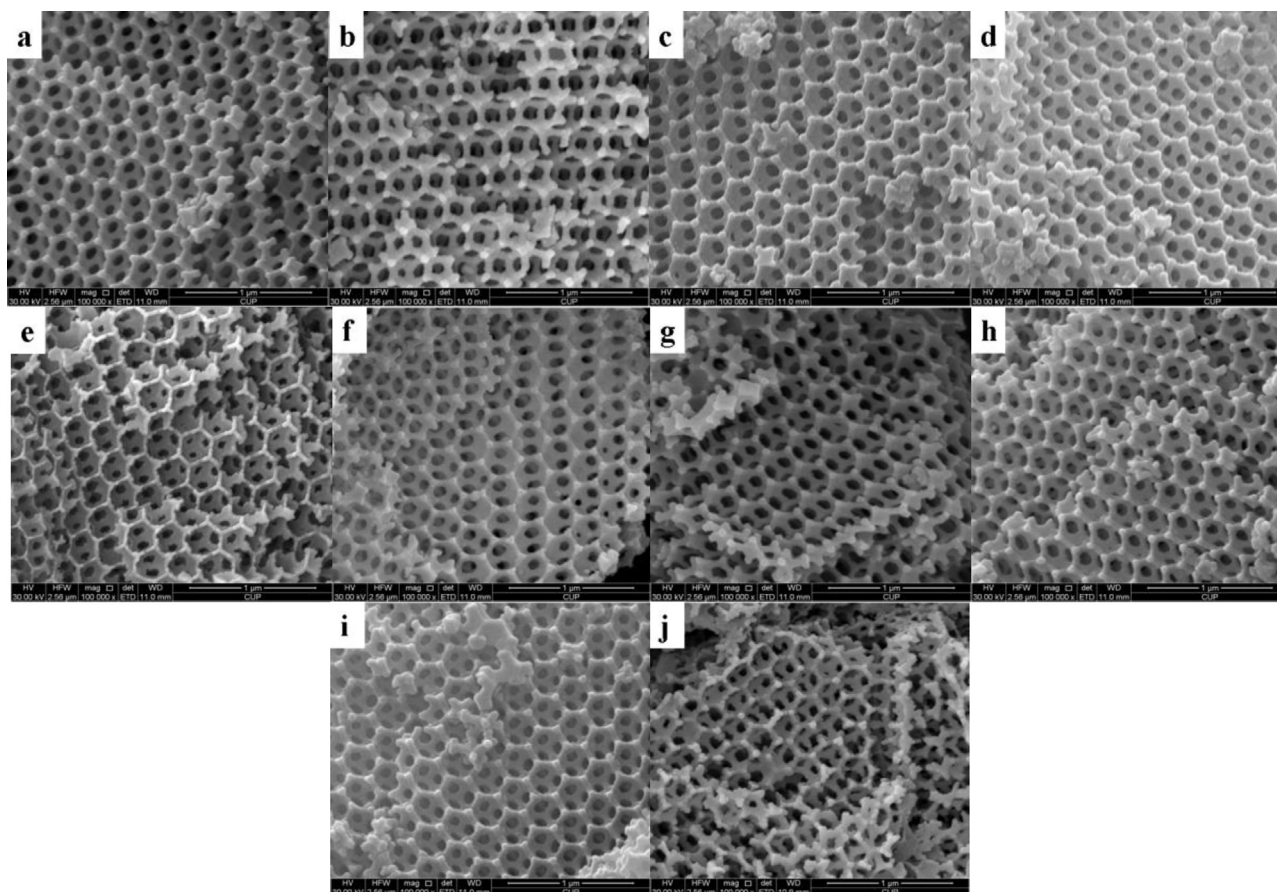
Fig. 3. SEM images of 3DOM TMO and Pt/TMO catalysts. a. Mn_2O_3; b. Pt/Mn_2O_3; c. Fe_2O_3; d. Pt/Fe_2O_3; e. Co_3O_4; f. Pt/Co_3O_4; g. NiO; h. Pt/NiO; i. CuO; j. Pt/CuO.

assigned to the open windows interconnected macropores in SEM images. It is also noted that the pore diameters (~6.0 nm) of all catalysts are observed, which may be assigned to the nanopores on the inner wall of 3DOM TMO supports. The total pore volumes and the average pore diameters of various concretes are analyzed and compared, and the results are given in Table 2. The total pore volume of the materials determined by N_2 physisorption (0.10–0.16 ml g^{-1}) is less than 5% of the total pore volume (2.9–3.6 ml g^{-1}) determined by MIP, indicating the main contribution of macropores to the total porosities in these materials. The porosities of 3DOM materials are beyond 90% due to the shrinkage during the sintering of the metal oxides, indicating that the solid reactants can easily diffuse into the materials and 3DOM structure is good at enhancing the catalytic activity for soot combustion.

Fig. 4(B and C) shows the representative nitrogen adsorption–desorption isotherm and pore size distribution curve

by BJH measurement of 3DOM Pt/TMO catalysts. It can be seen from Fig. 4(B) that a nearly linear correlation between the absorbed volume and relative pressure is observed under the low pressure in the relative pressure (p/p_0) range of 0–0.4, which is attributed to unrestricted monolayer–multilayer adsorption. A type IV nitrogen adsorption–desorption isotherms with a type H$_3$ hysteresis loop is presented in the relative pressure (p/p_0) range of 0.4–1.0, indicating that 3DOM Pt/TMO catalysts possess mesoporous structure, and a large rise of nitrogen adsorption-desorption isotherms in the relative high pressure (p/p_0) range of 0.8–1.0 is the characteristic of mesoporous structure origined from the nanoporous walls or the textural mesopores with tenuously assembled clusters. It suggests that 3DOM Pt/TMO catalysts prepared in this work possess microstructures with dual porosities containing the three-dimensionally ordered macropores and the mesopores. That is to say, there are a lot of mesopores or nanopores on the macropore

Table 2
Porosities, average diameters, pores volume and pore areas of 3DOM TMO and Pt/TMO catalysts with nanoporous walls determined by MIP and BET.

3DOM catalyst	A_p^a/m^2 g^{-1}	V_{Hg}^b/ml g^{-1}	D_p^c/nm	Porosity^d/%	S_{BET}^e/m^2 g^{-1}	V_p^f/ml g^{-1}	D_p^g/nm
Pt/Mn$_2$O$_3$	32.5	3.3	78.2	91.3	36	0. 12	6.6
Pt/Fe$_2$O$_3$	34.6	3.6	76.1	93.1	40	0.16	5.8
Pt/Co$_3$O$_4$	29.4	3.1	75.6	90.8	34	0.13	6.3
Pt/NiO	28.2	2.9	78.3	91.6	38	0.10	6.1
Pt/CuO	30.1	3.1	77.8	92.2	33	0.11	6.2

^{a} Total pore area determined by MIP.
^{b} Total pore volume for pores determined by MIP.
^{c} The median pore diameter determined by MIP.
^{d} Determined by Hg porosimetry.
^{e} Surface area obtained by BET method.
^{f} Pore volume determined by BET method.
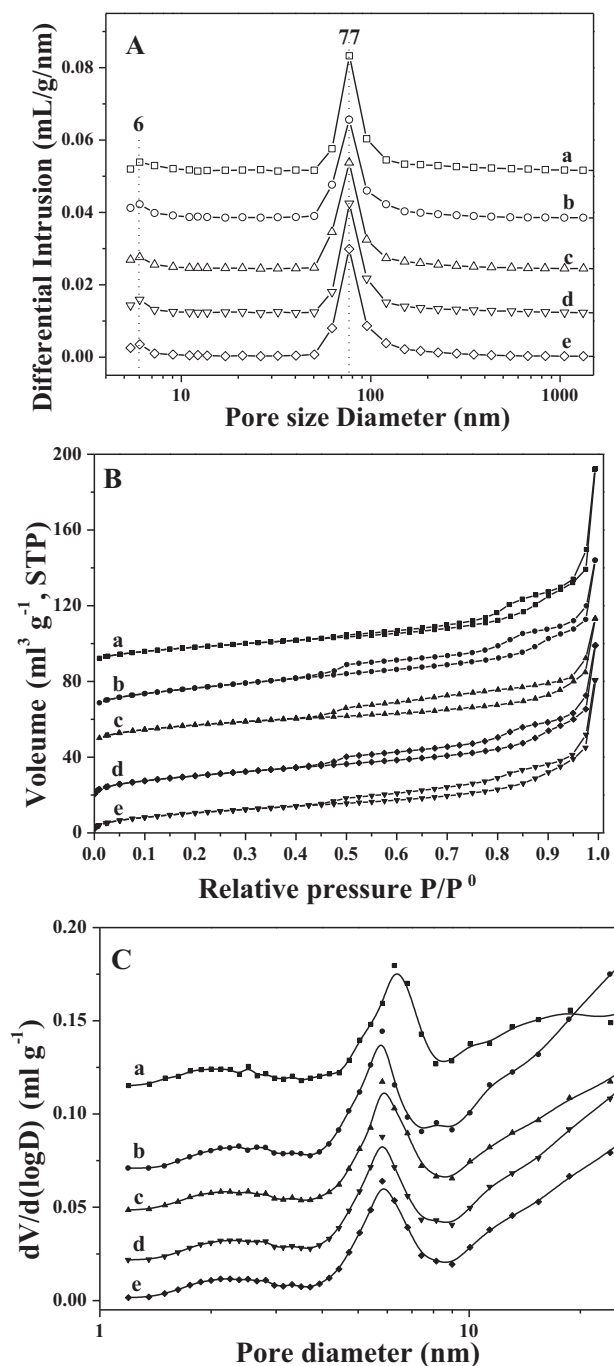^{g} The median pore diameter determined by BJH method.

Fig. 4. Pore size distribution determined by MIP (A), nitrogen adsorption–desorption isotherms (B) and pore size distribution plots determined by BJH measurement (C) of the 3DOM Pt/TMO catalysts with nanoporous walls. a. Pt/Mn$_2$O$_3$; b. Pt/Fe$_2$O$_3$; c. Pt/Co$_3$O$_4$; d. Pt/NiO; e. Pt/CuO.

walls of TMO supports. The corresponding mesopore size distribution shown in Fig. 4(C) indicates that the mesopore sizes of 3DOM Pt/TMO catalysts are dominantly distributed between 3.0 nm and 9.0 nm with a peak value at ~6.0 nm, which is in good agreement with MIP measurement. The BET surface areas and pore properties of 3DOM Pt/TMO catalysts are summarized in Table 2. The BET surface areas of the catalysts are 33.0–40.0 m^2 g^{-1}, and the median pore diameters determined by BJH method are 5.8–6.6 nm. 3DOM Pt/TMO catalysts with nanoporous walls will be hereafter considered as one of the suitable systems with the high catalytic activity for the combustion of solid particles.

3.4. The results of TEM and HRTEM characterizations

Fig. 5 shows TEM images of 3DOM Pt/TMO catalysts with nanoporous walls (M: Mn, Fe, Co, Ni, Cu). 3DOM structure with overlapped pores can be clearly observed. As shown in Fig. 5(a, c, e, g and i), the macropore diameter sizes of 3DOM TMO support in the catalysts are about 270 ± 10 nm, and the voids are interconnected through open windows with a diameter of 75 ± 5 nm, which is in agreement with the results obtained by SEM images and MIP. The wall of the typical 3DOM Pt/Fe$_2$O$_3$ catalyst is crystalline according to the selected area electron diffraction (SAED) image, as shown in inset of Fig. 5(c). The characteristic SAED rings are indexed as (0 1 2), (1 0 4), (1 1 0), (1 1 3) and (0 2 4) crystal faces of the rhombohedral structure of Fe$_2$O$_3$ support, and the characteristic SAED rings assigned to Pt nanoparticles are not detected. The perfect macroporous structure provides the ideal reaction space for solid reactants (diesel soot particles). The pore sizes of these catalysts are big enough to permit the model soot particles to enter their inner pores and reduce the diffusion resistance, and the number of contact points between soot and catalysts will be increased dramatically. As shown in Fig. 5(b, d, f, h and j), the magnified TEM images reveal the existence of nanoporous walls in all catalysts, and the sizes of the nanopores on the inner wall of 3DOM TMO supports are in the range of 5–10 nm. The nanopores on the skeletons of 3DOM TMO supports can increase the surface area, which leads to improving the capability of absorption and activation for gas reactant. In addition, we can note that all Pt nanoparticles with uniformed size are highly dispersed on the surface of 3DOM TMO supports with nanoporous walls, and the pore structure (3DOM and nanopores) of TMO supports (Fig. S4) have no apparent change after the deposition of Pt nanoparticles. Therefore, the catalytic activity of 3DOM Pt/TMO catalysts with nanoporous walls for soot combustion will be enhanced remarkably.

In order to further observe the nanoporous walls and Pt nanoparticles, HRTEM images and size distributions of Pt nanoparticles over 3DOM TMO supports (M: Mn, Fe, Co, Ni, Cu) are showed in Fig. 6. The nanopores (marked with white circle) on the walls of 3DOM TMO supports are composed of many mesopores resulting from the decomposition of soft template (P123). The sizes of the nanopores are estimated to be about 6.0 nm, which are well consistent with Barrett–Joyner–Halenda (BJH) pore size and volume analysis shown in Fig. 4(C). The supported Pt nanoparticles (marked with black circles) precipitated on the surface of 3DOM TMO supports can be clearly observed in HRTEM images of Fig. 6, and all Pt particles are highly dispersed and uniformed in size and morphology. The face angles of supported Pt nanoparticles are larger than 90° in inset of Fig. 6(a, e and i), indicating that Pt nanoparticles exhibited the morphology of truncated polyhedron with the high-index facets on the surface of the TMO supports. The tight contact angles between TMO supports and Pt nanoparticles are about 90°. It is evident that the roughness originated from the contact between the Pt nanoparticles and the TMO supports, which is an indication of the existence of a strong metal–support interaction at the atomic level [34]. The interaction between Pt and the TMO supports would be favorable for the mobility of lattice oxygen in the bulk of TMO support, and may be conducive to the production of oxygen vacancies on the surface of Pt/TMO catalysts [35]. The lattice fringes of truncated polyhedron Pt nanoparticles in HRTEM images were measured to be 2.3 Å indexed as (1 1 1) planes of fcc platinum nanoparticles in inset of Fig. 6(a, c and g). It indicates that supported truncated polyhedron Pt nanoparticles are crystalline and exposed fcc (1 1 1) planes, but the high-index facets of truncated polyhedron Pt nanoparticles is difficult to observe due to the small size (<7 nm) of Pt nanoparticles. The sizes of truncated polyhedron Pt nanoparticles over 3DOM TMO supports are in the range of 1–7 nm with a narrow size distribution, and the mean diameters
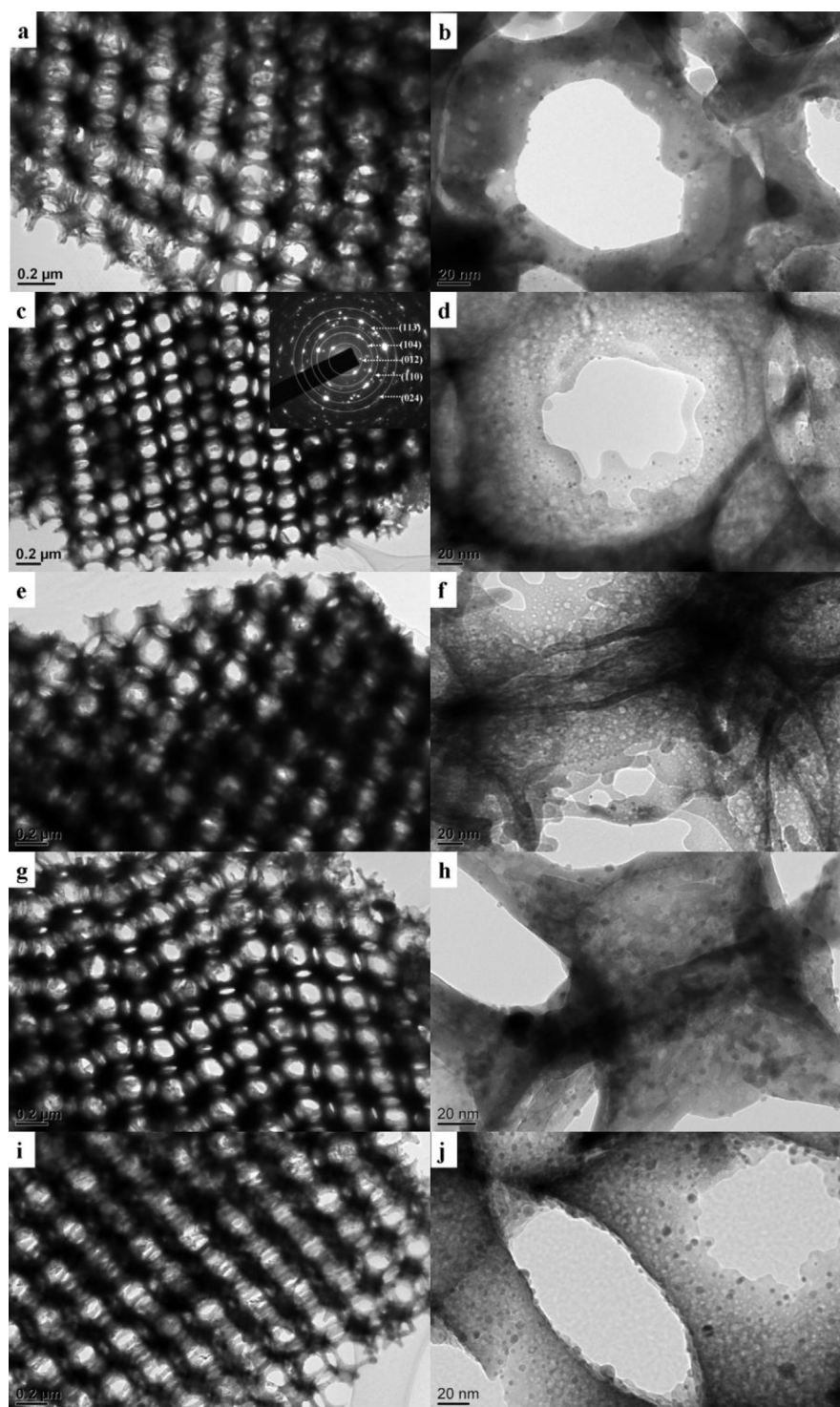
Fig. 5. TEM images of 3DOM Pt/TMO catalysts with nanoporous walls. The inset in c image is the corresponding SAED pattern of 3DOM Fe_2O_3 support. (a and b) Pt/Mn_2O_3; (c and d) Pt/Fe_2O_3; (e and f) Pt/Co_3O_4; (g and h) Pt/NiO; (i and j) Pt/CuO.

of truncated polyhedron Pt nanoparticles for all catalysts are 3.2 ± 0.3 nm by statistic analysis of more than 300 Pt particles for each sample, as shown in Fig. 6(b, d, f, h and j). The materials of nano-composite structure, between nanometric crystal of 3DOM TMO supports and truncated polyhedron Pt nanoparticles active component, should possess strong synergetic effect for enhancing the redox ability of catalysts [36]. The particle size and physical structure of the platinum nanoparticles are very similar in 3DOM Pt/TMO catalysts, indicating that the interference of size effect of

Pt particles may be ignored in the identification of the influence of the support on the catalytic activity.

3.5. The results of H_2-TPR

For metal oxide-based catalysts, H_2-TPR measurement can simultaneously reflect the reducibility of metallic ion from high valence to low valence or metallic atom, and the potential to remove or take up oxygen, i.e., the mobility and amount of the
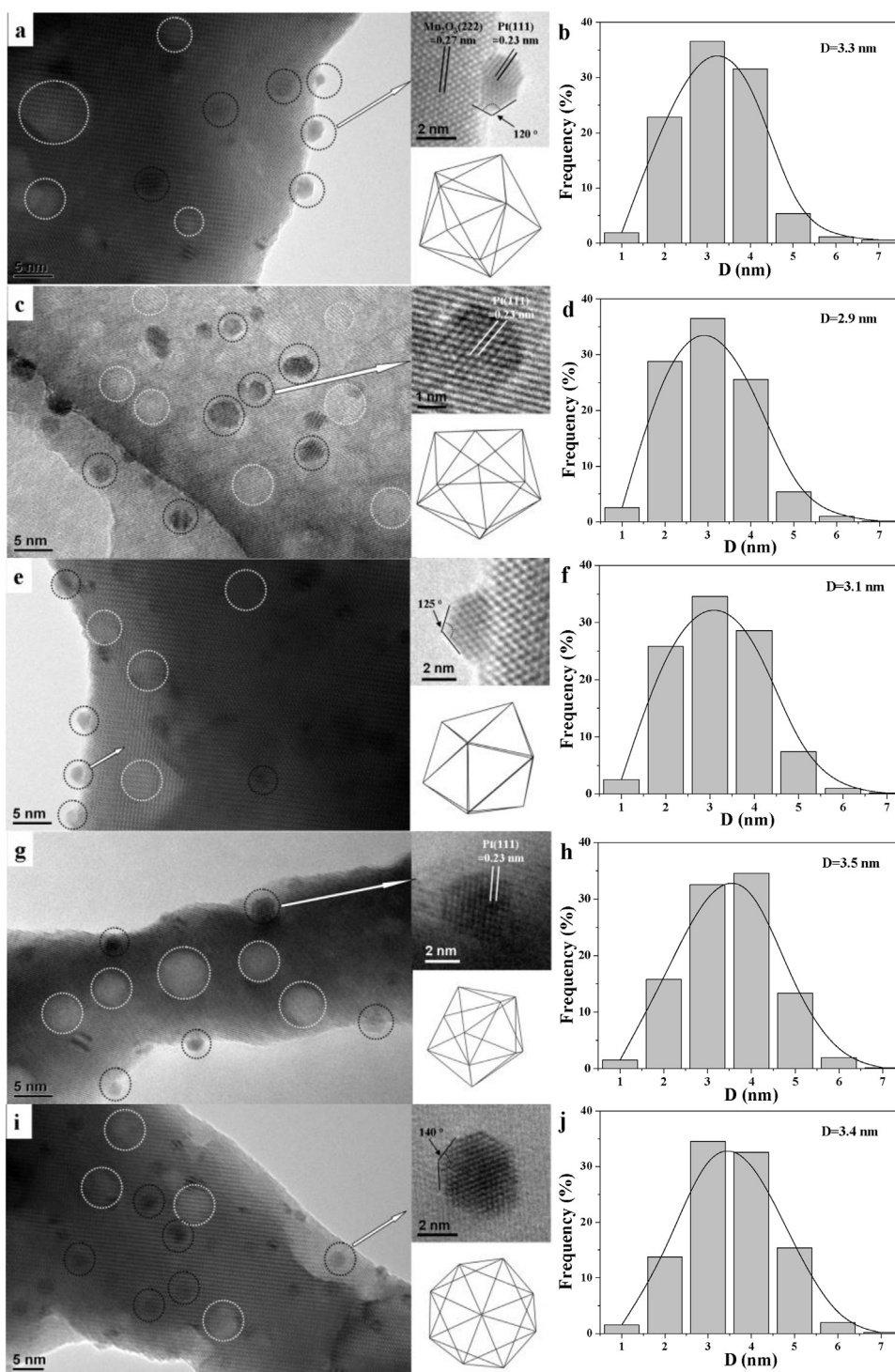
Fig. 6. The HRTEM images and size distributions of truncated polyhedron Pt nanoparticles over 3DOM TMO supports. The nanoporous on the surface of 3DOM TMO walls are marked with white circle, and the Pt nanoparticles are marked with black circles. The ones in inset of (a, c, e, g and i) images show truncated polyhedron Pt nanoparticle whose lattice fringes correspond to fcc (1 1 1) plane at 2.3 Å. (a and b) Pt/Mn$_2$O$_3$; (c and d) Pt/Fe$_2$O$_3$; (e and f) Pt/Co$_3$O$_4$; (g and h) Pt/NiO; (i and j) Pt/CuO.

surface oxygen species [37]. In this work, the temperature and intensity of reduction (T_{red}) peaks are taken as a measure to evaluate the redox ability of catalyst. It is general known that there are four kinds of reduction peaks on the H$_2$-TPR curves of all samples, namely, $\alpha(T_{red} < 150\,°C)$, $\beta(150\,°C < T_{red} < 300\,°C)$, $\gamma(300\,°C < T_{red} < 550\,°C)$ and $\delta(T_{red} > 550\,°C)$, which are attributed to a physisorptions' or weak chemisorptions' oxygen species, a less negatively charged species O$_2^-$, a more negatively charged species O$^-$ and the lattice oxygen O^{2-}, respectively [38]. The lower the

T_{red} is, the stronger the reducibility of catalyst is. Since in practical applications the catalytic combustion of diesel soot particles occur in the temperature range of 200–500 °C, we especially focus on the β and γ reduction peaks in H$_2$-TPR measurements. The deconvolution of the H$_2$-TPR profiles of 3DOM TMO and Pt/TMO catalysts are shown in Fig. 7, and the amounts of H$_2$ consumption for the each peak and the total amounts of H$_2$ consumption for all the peaks with different temperatures on 3DOM TMO and Pt/TMO catalysts are shown in Table S1. With the difference of
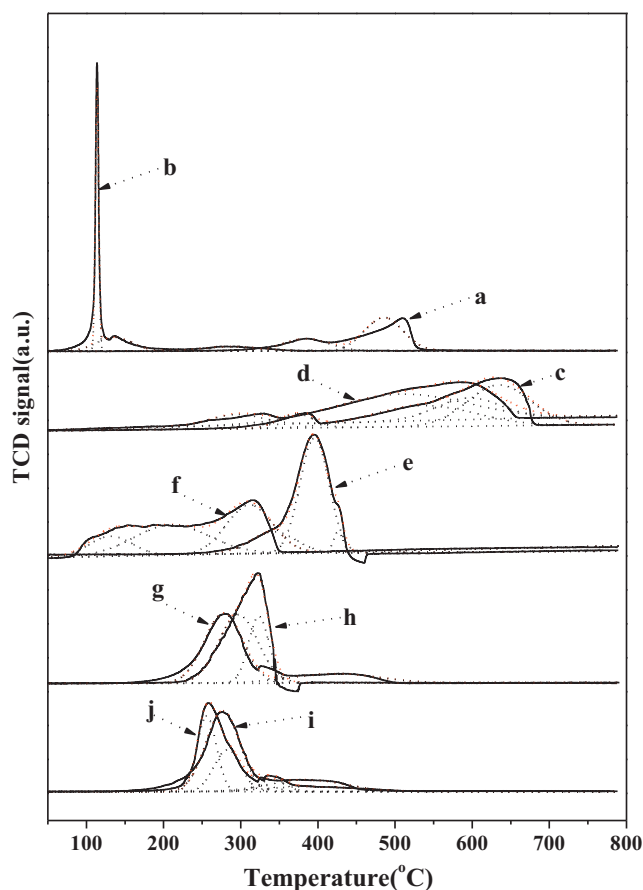
Fig. 7. The H_2-TPR profiles of 3DOM TMO and Pt/TMO catalysts with nanoporous walls. a. Mn_2O_3; b. Pt/Mn_2O_3; c. Fe_2O_3; d. Pt/Fe_2O_3; e. Co_3O_4; f. Pt/Co_3O_4; g. NiO; h. Pt/NiO; i. CuO; j. Pt/CuO.

of 200–550 °C, indicating that the reducibility of Fe- and Co-based catalysts enhanced. The considerable decrease in the reduction temperature of Fe- and Co-based catalysts might be due to a certain amount of Pt oxide species have been introduced into metal oxide lattice in the form of Pt-O-metal bonds, thus resulting in spillover of atomic hydrogen from Pt to the oxide surface occurs more easily [39]. In the H_2-TPR profiles of 3DOM Pt/NiO (NiO) and 3DOM Pt/CuO (CuO) catalysts, the position of the strong reduction peaks of Ni- and Cu-based catalysts almost does not change. However, the breadth of reduction peaks obviously narrowed and the total hydrogen consumption increased slightly. It suggests that the reducibility of Ni- and Cu-based catalysts did not obviously change after the deposition of truncated polyhedron Pt nanoparticles. It is reasonable to suppose that the interactions between NiO/CuO and Pt nanoparticles are weak in contrast to the interaction between Fe_2O_3 or Co_3O_4 and Pt nanoparticles [41]. According to the results of H_2-TPR measurements, we can conclude that the interaction between Pt nanoparticles and TMO (M: Mn, Fe, Co, Ni, Cu) is decreasing with the increasing of atomic number, but the interaction with too strong or too weak is disadvantageous to the improvement of redox ability. Among these catalysts, 3DOM Pt/TMO (M: Fe, Co) catalysts display the better redox property compared to the others in the temperature region of 200–550 °C, indicating that they will have better catalytic performance for soot combustion.

3.6. The results of XPS

Generally speaking, the catalytic performance of materials for deep oxidation reaction correlates with the capability of oxygen activation. To examine the electronic properties of the supported Pt nanoparticles and surface oxygen species, 3DOM TMO and Pt/TMO catalysts with nanoporous walls were studied by XPS, and the results are shown in Fig. 8. As shown in Fig. 8(A), the deconvolution of the Pt 4f XPS spectra of 3DOM Pt/TMO catalysts were made by the standard procedure, and the binding energies of 71.0 and 74.3 eV, 72.2 and 75.7 eV, 74.8 and 77.8 eV have been assigned to Pt^0, Pt^{2+} and Pt^{4+} species, respectively, indicating that both metallic and ionic platinum species are present on 3DOM Pt/TMO catalysts. It may also reflect the stabilization of PtO and/or PtO_2 on Pt^0 particles or the presence of oxygen species. The ion states of platinum species ($Pt^{\&+}$) are considered to be the more active than the metal state (Pt^0) for oxidation reaction [42]. In addition, the Cu $3P_{1/2}$ and Cu $3P_{3/2}$ binding energies of 3DOM Pt/CuO catalyst located at 77.0 and 75.0 eV, respectively, which can disturb the observation of Pt 4f binding energies. It is clearly noted that the ratios of platinum species ($Pt^{\&+}$) in the Pt species over the surface of TMO supports are obviously different, indicating that there is a discriminatory the strong interaction between TMO supports and Pt nanoparticles which may lead to transference of the lattice oxygen in TMO to the surface of Pt nanoparticles and maintain platinum at the high-valent state [43]. Therefore, it is noted that the strong Pt–TMO interaction is dependent on the nature of TMO supports. In order to determine the effect of TMO supports on the valent state of Pt nanoparticles, we estimated the relative amount of each Pt species (Pt^0, Pt^{2+} and Pt^{4+}) on the surface of catalyst by the deconvolutions of XPS spectra and the results are presented in Table S2. Among 3DOM Pt/TMO catalysts with nanoporous walls, 3DOM Pt/Mn_2O_3 catalyst possesses the largest Pt species ratio of $Pt^{\&+}$ to Pt^0 (R^a) about 7.17, indicating that the platinum atoms over the surface of Mn_2O_3 mainly bear a positive charge due to the strong metal(Pt)–support(Mn_2O_3) interaction. With the increasing of atomic number of TMO supports, the R^a value decreases from 7.17 (Mn_2O_3) to 0.79 (NiO), which is probably due to the weak strength of the metal(Pt)–support(Mn_2O_3) interaction (Table S2). The formation of a Pt–O–Metal bond would decrease the total energy of Pt/TMO and then stabilize Pt species dispersed on the

TMO supports, the changed reducibility of the catalysts makes a difference after the introduction of truncated polyhedron Pt nanoparticles on the surface of 3DOM TMO with nanoporous walls. For 3DOM Mn_2O_3 support, there are two apparent reduction peaks located at ∼384 and ∼484 °C which are attributed to the removal of a small amount of adsorbed oxygen species and the reduction of Mn^{3+} to Mn^{2+}, respectively. After introduction of truncated polyhedron Pt nanoparticles, however, the strong reduction peaks are apparent shifted to the lower temperature located at ∼114 and ∼137 °C which are typical α-type reduction peaks. It indicates that the mobility and activation of oxygen species over the surface of supported Pt catalysts are enhanced because of the strong metal(Pt)–support(Mn_2O_3) interaction. And the reduction peaks at 200–400 °C almost complete disappear, indicating that the ability of oxygen storage and absorption become weak at this temperature.

In the H_2-TPR profiles of 3DOM Pt/Fe_2O_3 (Fe_2O_3) and 3DOM Pt/Co_3O_4 (Co_3O_4) catalysts, the reduction peaks after introducing Pt nanoparticles remarkably shift to lower temperature than those of bare metal oxides. For Fe-based catalysts, the strong and broad reduction peaks appeared at ∼372, ∼537 and ∼634 °C could be mainly attributed to the reduction transformation of bulk Fe_2O_3 to Fe_3O_4, Fe_3O_4 to FeO and FeO to metallic Fe, respectively [39]. The H_2-TPR profile of pure Co_3O_4 crystalline shows a shoulder peak at ∼342 °C and a reduction peak centered at ∼396 °C which were attributed to the reduction processes of $Co^{3+} \rightarrow Co^{2+}$ and $Co^{2+} \rightarrow Co^0$, respectively [40]. After introduction of truncated polyhedron Pt nanoparticles, the strong reduction peaks of Fe- and Co-based catalysts were apparently shifted to the lower temperature and the total hydrogen consumption increased at the region
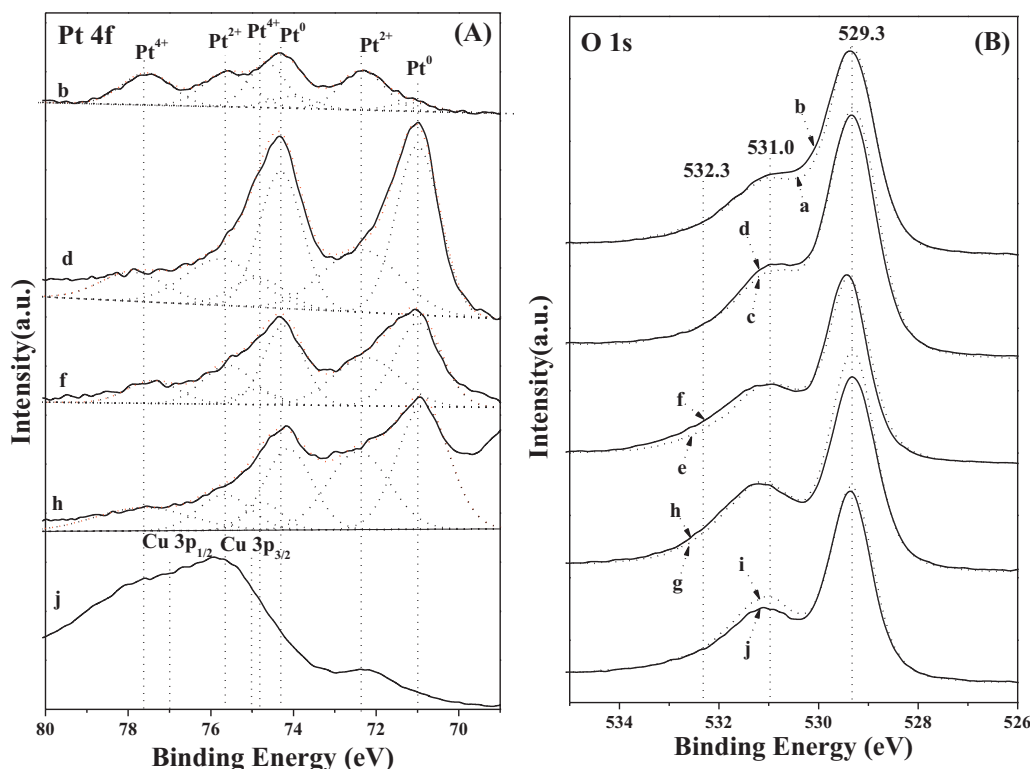
Fig. 8. XPS spectra of Pt 4f (A) and O 1s (B) regions for 3DOM TMO and Pt/TMO catalysts with nanoporous walls. a. Mn_2O_3; b. Pt/Mn_2O_3; c.Fe_2O_3; d. Pt/Fe_2O_3; e. Co_3O_4; f. Pt/Co_3O_4; g. NiO; h. Pt/NiO; i. CuO; j. Pt/CuO.

support [44]. Hence, it is deduced that the appearance of $Pt^{\&+}$ species may lead to the increased amount of surface active oxygen species (O_2^-, O^-), which is originated from the decrease in the d-electron density of the Pt atoms and the onset of reactivity to oxygen in the air [45].

As shown in Fig. 8(B), the O 1s binding energies locate at 529.3, 531.0 and 532.3 eV, which are assigned to lattice oxygen species (O^{2-}) and active oxygen species (O_2^{2-} and O_2^-), respectively [30,46]. It indicates that the active oxygen species are present on the surface of 3DOM TMO and Pt/TMO catalysts. The O 1s XPS spectral lines of 3DOM Pt/TMO catalysts (full lines) are slightly different from that of 3DOM TMO catalysts (dotted lines). In order to investigate the effect of Pt nanoparticles on the surface oxygen species, the deconvolution of the O 1s XPS spectra of 3DOM TMO and Pt/TMO catalysts were made by the standard procedure and the results are shown in Fig. S6 and Table S2. It can be seen that the content ratios of $O_2^{\&-}$ in supported Pt nanoparticles catalysts remarkably increase in contrast to the bare TMO supports except for Cu-based catalysts. It indicates that the supported-Pt particles can enhance the capability of oxygen activation and increase the amount of surface active oxygen species (O_2^-, O^-), which would give rise to unusual catalytic properties for deep oxidation reaction. Among 3DOM Pt/TMO catalysts with nanoporous walls, the R^b value (the oxygen species ratio of O_2^- and O_2^{2-} to O^{2-}) of 3DOM Mn-based catalysts is the largest, in other words, the R^b value of 3DOM Pt/Mn_2O_3 catalyst is 0.90 while that of 3DOM Mn_2O_3 catalyst is 0.68. And with the increasing of atomic number of supports, the variation of R^b values decreased. In our previous works, we have found that the catalytic performances of supported noble metal catalysts are strongly related to the role of supports including the structures and the active oxygen supply pathways [27]. Therefore, it can be deduced that there is strong interaction between Pt nanoparticles and TMO, and the strength of Pt–Mn_2O_3 interaction is stronger than that of Pt–CuO interaction. The strong interaction between Pt nanoparticles and

TMO supports can lead to the electron transference from metallic Pt to metal cations, and the distribution of electronic charges between a small cluster of Pt atoms and support can weaken the M–O bond and increase the amount of active oxygen species [47]. Finally, the reducibility of 3DOM Pt/TMO catalysts with nanoporous walls are improved, which is in good agreement with those of H_2-TPR measurements.

3.7. The results of NO oxidation

In the well-known NO_2-assisted mechanism of catalytic combustion for diesel soot particles, NO_x was used as an efficient mobile oxidizing agent that accesses the soot and causes light-off of soot in an appropriate temperature range, because NO_2 is a kind of much more effective oxidant than O_2 [2]. But most of NO_x in diesel exhaust gas is NO, the content of NO_2 is little. Therefore, it is also important to improve the activation capability of the catalysts for gas reactant (O_2 and NO) [48]. To clearly observe the concentration of NO_2 derived from NO oxidized over typical 3DOM Pt/Fe_2O_3 catalyst with nanoporous walls, the NO oxidation experiments were performed and the results are shown in Fig. 9. For comparison, the NO_2 concentration profiles of NO oxidation over 3DOM Fe_2O_3 support, 3DOM Pt/Fe_2O_3-NNP catalyst and the case without catalyst are also included. Almost no NO_2 was detected in the case without catalyst at temperatures below 500 °C, as shown in the plot (a). However, when 3DOM TMO catalyst was present, the NO_2 concentration peak is clearly detected by the means of MS, as shown in plot (b). After introduction of truncated polyhedron Pt nanoparticles, the NO_2 concentration curve (d) of 3DOM Pt/Fe_2O_3 catalyst with nanoporous walls is higher and wider than that (c) of 3DOM Pt/Fe_2O_3-NNP catalyst, indicating that the nanopores on the inner wall of 3DOM supports is favorable for improving the activation capability of the catalysts for gas reactant (O_2 and NO). It may partially explain the reason that 3DOM Pt/Fe_2O_3 catalyst with
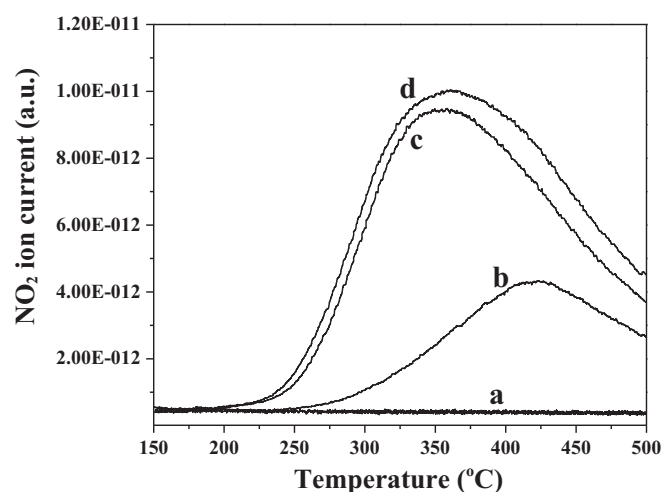
Fig. 9. The ion current curves for outlet NO_2 during NO oxidation process detected by mass spectrometry. (a) Without catalyst; (b) 3DOM Fe_2O_3; (c) 3DOM Pt/Fe_2O_3-NNP; (d) 3DOM Pt/Fe_2O_3.

nanoporous walls exhibit high catalytic activity for soot combustion. In addition, the NO_2 concentration obtained from the catalysts does not increase with temperature rising until the thermodynamic equilibrium of the equation ($NO + 1/2O_2 \leftrightarrow NO_2$) was fulfilled, and then decreases at higher temperatures and follows thermodynamic profile.

3.8. Catalytic activity for soot combustion

The catalytic activities of 3DOM TMO and Pt/TMO catalysts with/without nanoporous walls for soot combustion were evaluated by TPO method using NO/O_2 mixtures as oxidizing agents and the results are listed in Table 3 and Fig. S7. For comparison, the TPO result of bare soot (i.e., without catalyst) is also included. As shown in Fig. S7(A), 3DOM TMO catalysts with nanoporous walls have high catalytic activity for soot oxidation, which is attributed to the open and interconnected macropore structure giving more contact area between soot particles and catalysts under the condition of soot embedded into the inner pores with the help of airflow. The catalytic activity for soot oxidation is remarkably enhanced after the introduction of truncated polyhedron Pt nanoparticles on the surface of 3DOM TMO supports except for Mn-based catalysts. The peaks of CO_2 concentration profiles for soot combustion over 3DOM Pt/TMO catalysts shift to the lower temperature (centered range in 320–380 °C) comparing with those of 3DOM TMO catalysts (at ~450 °C). As shown in Fig. S7(B), the selectivity of CO_2 (S_{CO_2}) in the soot combustion over 3DOM Pt/TMO catalysts with nanoporous walls are remarkably improved in contrast to 3DOM Pt/TMO catalysts without nanoporous walls (Pt/TMO-NNP). It is attributed to the nanoporous walls giving more choice for the contact between CO molecule and catalyst. The S_{CO_2} of 3DOM Pt/TMO-NNP catalysts were always less than 98%, and the higher values of S_{CO_2} are in narrow temperature range (250–400 °C). However, the S_{CO_2} is largely enhanced after introduction of the nanoporous walls on the surface of 3DOM Pt/TMO catalysts, and it is nearly 100% in a wide temperature range (200–450 °C), which can ensure that the CO emitted from cars is immediately removed under the practical temperature of diesel engine emissions (150–400 °C). And the S_{CO_2} of the 3DOM Pt/TMO catalysts are influenced by the supports with the different atomic number. The obvious difference in catalytic activity of 3DOM TMO and Pt/TMO catalysts with/without nanoporous walls for soot combustion can be more clearly observed in Table 3. For the bare soot (without catalyst), T_{10}, T_{50}, T_{90} and $S_{CO2}{}^m$ are 482, 585, 646 °C and 55.6%, respectively. The nanopores on the wall of TMO supports can improve the catalytic activity for soot combustion, which is in agreement with the higher capability of 3DOM Pt/TMO catalysts with nanoporous walls for NO oxidation than that of 3DOM Pt/TMO-NNP catalysts. Among 3DOM TMO and Pt/TMO catalysts with/without nanoporous walls, 3DOM Pt/Fe_2O_3 and Pt/Co_3O_4 catalysts exhibit the better catalytic activity than the others under loose contact condition. For instance, the T_{50} of 3DOM Pt/Fe_2O_3 and Pt/Co_3O_4 catalysts are 358 and 351 °C, respectively. 3DOM Pt/Co_3O_4 catalyst with nanoporous walls is one of the Pt-based catalysts with high activity for soot combustion in the reported results under the same/similar conditions (Table S3). It might be assigned to the fact that the synergetic effect between Pt nanoparticle and Fe_2O_3/Co_3O_4 carrier could improve the capability of dioxygen activation. Furthermore, it is also found that there is a negative effect on the catalytic activity of Mn-based catalysts after introduction of the Pt nanoparticles. For example, the ΔT_{50} value of 3DOM Fe-based catalysts with nanoporous walls is the largest with 84 °C, while that of 3DOM Mn-based catalysts is −30 °C. In conclusion, it suggests that the catalytic activity of 3DOM TMO supported Pt nanoparticles catalysts could be strongly related to the structure and composition of TMO supports and the strong interaction between Pt nanoparticles and TMO.

The thermal stability of typical 3DOM Pt/Fe_2O_3 catalyst with nanoporous walls was further examined by consecutive soot

Table 3
The temperatures and the selectivity to CO_2 of soot combustion over 3DOM TMO and 3DOM Pt/TMO catalysts and without catalyst (loose contact).

Catalyst (3DOM)	T_{10}/°C	T_{50}/°C	T_{90}/°C	$S_{CO_2}^m$/%	$\Delta T_{50} = T_{50}{}^a - T_{50}{}^b$/°C
Without catalyst	482	585	646	55.6	–
Mn_2O_3[a]	293	366	412	99.8	
Pt/Mn_2O_3[b]	318	396	450	99.9	−30
Pt/Mn_2O_3-NNP[c]	320	401	454	96.9	
Fe_2O_3[a]	362	442	488	82.9	
Pt/Fe_2O_3[b]	286	358	401	99.8	84
Pt/Fe_2O_3-NNP[c]	292	360	404	97.8	
Co_3O_4[a]	338	427	482	97.8	
Pt/Co_3O_4[b]	285	351	396	98.5	66
Pt/Co_3O_4-NNP[c]	284	353	399	96.5	
NiO[a]	367	448	485	97.3	
Pt/NiO[b]	302	381	403	98.6	57
Pt/NiO-NNP[c]	305	386	406	96.5	
CuO[a]	356	438	471	96.9	
Pt/CuO[b]	353	411	446	98.3	27
Pt/CuO-NNP[c]	352	412	448	96.3	

[a] 3DOM TMO catalysts with nanoporous walls.
[b] 3DOM Pt/TMO catalysts with nanoporous walls.
[c] 3DOM Pt/TMO catalysts without nanoporous walls.

Table 4
Stability test results of 3DOM Pt/Fe$_2$O$_3$ catalyst with nanoporous walls for soot combustion under the condition of loose contact between catalyst and soot used for five cycles.

Test cycles[a]	$T_{10}/°C$	$T_{50}/°C$	$T_{90}/°C$	$S_{CO2}^m/\%$
1st	286	358	401	99.8
2nd	287	357	399	99.6
3rd	285	357	402	99.8
4th	288	359	401	99.6
5th	287	358	400	99.8

[a] Reaction gas, 5% O$_2$ and 0.2% NO in Ar, 50 ml min^{-1}.

combustion for five cycles, and the TPO results are shown in Table 4. 3DOM Pt/Fe$_2$O$_3$ catalyst with nanoporous walls maintains its high catalytic activity and $S_{CO_2}^m$ for five cycles of TPO experiments under the condition of loose contact between catalysts and soot particles, i.e., the numerical values of T_{50} and $S_{CO_2}^m$ are 358 ± 1 °C and ~100%, respectively. According to the SEM and TEM images of 3DOM Pt/Fe$_2$O$_3$ catalyst with nanoporous walls used for five cycles in Fig. S8, 3DOM structure is not destroyed after the TPO experiment, and the mean size (3.0 nm) of Pt nanoparticles on the surface of the 3DOM Fe$_2$O$_3$ support is not remarkably changed in comparison with that of the fresh sample (2.9 nm). The result indicates that 3DOM TMO-supported Pt catalysts have good thermal stability for soot combustion reaction.

4. Discussion

The catalytic combustion of diesel soot particle is a typical heterogeneous catalytic reaction, which takes place at the three-phase boundary among a solid catalyst, a solid reactant (soot) and gaseous reactants (O$_2$, NO). The efficiency of catalyst for solid–solid reaction is strongly influenced by the contact between soot and catalyst in the process of catalysis. In many studies, the catalytic performances for soot combustion are very excellent under tight contact conditions between soot and catalyst because of their good contact [49]. However, in fact it is loose contact between active site of the catalysts and soot particles under practical conditions. Since the number of contact site is proportional to the active sites concentration, one can expect an increase in the activity with the higher surface area. The structures of catalysts can influence the catalytic activity for soot combustion. Thus, it is significantly important to study and design the active catalysts which improve the contact efficiency between the catalysts and soot particles under loose contact conditions. To meet the increasing needs of contact area, 3DOM materials with nanoporous walls and periodic voids inter-connected through open windows are designed and synthesized by the surfactant (P123)-assisted colloidal crystal template method. In this work, 3DOM Pt/TMO catalysts with nanoporous walls have high catalytic activity for soot combustion. In our pervious works, it has been proved that soot particles can easily enter the interior of 3DOM catalysts with the help of the airflow in the reaction process under the loose contact conditions, and have less resistance to go through the catalyst structure [26,50]. The contact efficiency between soot and catalyst is improved in the reaction process. However, 3DOM structure is unfavorable for improving the selectivity of CO$_2$ production, because the large amounts of CO is produced during soot combustion, and the small molecule of CO is possible to rapidly pass through 3DOM-based catalysts with the big pore and then gives fewer choices for the contact between CO and catalyst. But 3DOM Pt/TMO catalysts with nanoporous walls exhibit much higher S_{CO_2} in soot oxidation as shown in Table 3, which is easy for understanding that the increasing of the surface area is favorable for improving the contact between CO and catalyst. Therefore, 3DOM Pt/TMO catalysts with nanoporous walls
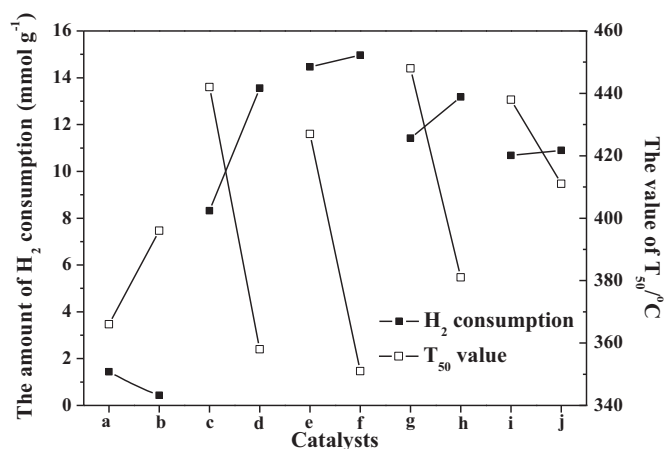

Fig. 10. The relation between the amount of H$_2$ consumption (150–550 °C) by H$_2$-TPR and the catalytic activity (T_{50}) for soot combustion over 3DOM Pt/TMO catalysts with nanoporous walls. a. Mn$_2$O$_3$; b. Pt/Mn$_2$O$_3$; c.Fe$_2$O$_3$; d. Pt/Fe$_2$O$_3$; e. Co$_3$O$_4$; f. Pt/Co$_3$O$_4$; g. NiO; h. Pt/NiO; i. CuO; j. Pt/CuO.

exhibit super catalytic performances for soot combustion except for Mn-based catalysts.

The structural feature of catalyst is only one of the controlling factors for enhancing the catalytic activity for the combustion of diesel soot particles. Since the reaction of soot combustion is a kind of deep oxidation reaction, the nature of the catalytic reaction is a redox process. Therefore, the intrinsic catalytic activities of 3DOM Pt/TMO catalysts with nanoporous walls are related to the redox property of themselves. Indeed, the reducibilities of 3DOM TMO and Pt/TMO catalysts were checked by H$_2$-TPR technique. 3DOM TMO as an appropriate supports show good redox property. The effectiveness of the catalysts is related to their ability to deliver oxygen from the lattice to the gas phase or the surface of soot particles in a wide temperature region, and TMO support has a strong ability to donate oxygen for soot oxidation. After introduction of truncated polyhedron Pt nanoparticles, the strong reduction peaks of all the catalysts gradually shift to lower temperature in Fig. 7, and the amount of H$_2$ consumption for the lower T_{red} peaks ranging from 50 to 550 °C increases except for Mn-based catalyst. It indicates that the mobility of lattice oxygen and the reducibility of 3DOM Pt/TMO catalysts are improved. Generally speaking, the catalytic performance of Pt-based catalysts strongly depends on the amount of active oxygen species. It is not the first time to report that the role of oxygen is evoked particularly in oxidation reactions over platinum nanoparticles [36]. The increase in the amount of "active oxygen species" induced by Pt cation can explain the good redox property of 3DOM Pt/TMO catalysts. In practical applications the catalytic combustion of diesel soot particles occurs in the temperatures range of 150–550 °C, therefore, we focus on the amount of H$_2$ consumption (150–550 °C) corresponding to the β and γ reduction peaks in H$_2$-TPR measurement. The relationship between the catalytic activities (T_{50}) of 3DOM Pt/TMO catalysts and the amount of H$_2$ consumption of the reduction peaks (150–550 °C) is shown in Fig. 10. The catalytic activities (T_{50}) of 3DOM Pt/TMO catalysts for soot combustion are closely related to the amount of surface-active oxygen species in the catalysts obtained by the amount of H$_2$ consumption of the lower T_{red} peaks (β and γ) in Table S1. 3DOM Pt/Co$_3$O$_4$ catalysts with the largest H$_2$ consumption exhibited the highest catalytic activity for soot combustion, and 3DOM Pt/Mn$_2$O$_3$ catalyst with the less H$_2$ consumption exhibited the lower catalytic activity for soot combustion in contrast to 3DOM Mn$_2$O$_3$ catalyst. On the basis of the experimental observations of H$_2$-TPR and XPS measurements, it can be deduced that the active oxygen species over 3DOM Pt/TMO catalysts are derived from the induced

support, which may result from the fact that TMO supports serve as a reservoir for oxygen in the oxidation reaction [32,51]. The strong interaction between TMO and Pt nanoparticles may lead to a transfer of the lattice oxygen from TMO supports to the surface of Pt nanoparticles at the low temperature, however, the interaction with too strong or too weak is disadvantageous to the improvement of catalytic activity for soot combustion. Among these catalysts, 3DOM Pt/TMO (M: Fe, Co) catalysts display the good redox property during the temperature region of 150–550 °C, which is consistent with their high catalytic activity for soot combustion.

Based on the above results and discussion, the following two reasons can determine the high catalytic activities of 3DOM Pt/TMO catalysts with nanoporous walls for soot combustion. First of all, new chemical phenomena may appear in nanostructural materials. The number of contact sites between catalysts and soot particles is a crucial factor affecting the catalytic performance for soot combustion. The contact between catalyst and soot is a necessary external condition which is significantly important for the typical reaction of heterogeneous catalysis containing solid particles as a reactant. Based on previous studies on the characterization of structure, 3DOM is a desirable structure for diesel soot combustion. The soot particles can diffuse into the inner pores of 3DOM catalysts, and the surface areas of inner pores reach a maximal application [27]. The direct contact between 3DOM catalysts and soot particles is a foundation condition for the migration of active oxygen species from catalyst to soot particle [52]. And the nanopores on the inner walls of 3DOM TMO supports are favorable for the improvement of the catalytic selectivity to CO_2 for soot combustion, which avoids secondary pollution and suppresses emission of CO. Secondly, the nature of soot oxidation is the redox process. The redox property of catalyst determines its intrinsic activity. The nano-composite structure materials, both nanometric crystal of TMO support and Pt nanoparticles active component, possess the strong redox ability. It is attributed to that TMO supports deliver oxygen from the lattice of bulk to the surface of material in a wide temperature region, and supported Pt nanoparticles can improve the redox ability due to the interaction between Pt nanoparticles and TMO supports. According to the result of H_2-TPR measurements, we can conclude that the interaction between Pt nanoparticles and TMO (M: Mn, Fe, Co, Ni, Cu) is decreasing with the increasing of atomic number, but the interaction with too strong or too weak is disadvantageous to the improvement of redox ability. Among these catalysts, 3DOM Fe_2O_3 and Co_3O_4 with nanoporous walls-supported truncated polyhedron Pt nanoparticles catalysts display better redox property and higher catalytic activity for soot combustion compared to the others. In summary, 3DOM Pt/TMO catalysts with nanoporous walls, which combine both advantages of the high contact efficiency by the structural effect of 3DOM supports with nanoporous walls and the abundant active oxygen species by the moderate interaction between TMO support and Pt nanoparticles, exhibited high catalytic activity for diesel soot combustion.

5. Conclusions

A series of 3DOM TMO supports (M: Mn, Fe, Co, Ni, Cu) with nanoporous walls were successfully prepared by the surfactant (P123)-assisted colloidal crystal template method, and 3DOM TMO-supported truncated polyhedron Pt nanoparticle catalysts were synthesized by GBMR method. 3DOM TMO supports with nanoporous walls are highly ordered and the voids are interconnected through the open window with the diameter of 80 ± 5 nm. The nanopores with the average size of ~6 nm and truncated polyhedron Pt nanoparticles with the average sizes of 2.9–3.5 nm are highly dispersed on the inner walls of uniform macropores. 3DOM Pt/TMO catalysts with nanopores walls exhibit the large total pore

volume (~3.4 ml g^{-1}), the high porosity (>91%) and surface area (36–40 m^2 g^{-1}).

The structure and composition of supports were found to have significant effects on the catalytic activity of 3DOM Pt/TMO catalysts for soot combustion. The strong metal (Pt)–support (TMO) interaction is favorable for the improvement of reducibility and for increasing the amount of active oxygen species. However, the too strong or too weak reducibility is disadvantageous to the improvement of catalytic activity for soot combustion. Among 3DOM Pt/TMO catalysts with nanoporous walls, Fe- and Co-based catalysts with the moderate reducibility exhibited higher catalytic activity for diesel soot combustion in contrast to the others. For instance, the T_{50} of 3DOM Pt/Fe_2O_3 and Pt/Co_3O_4 catalysts are 358 and 351 °C, respectively. And the nanopores on the inner walls of 3DOM TMO supports remarkably enhance the catalytic activity and selectivity for soot oxidation. The S_{CO_2} is nearly 100% in a wide temperature range (200–550 °C), which can ensure that the CO emitted from cars is immediately removed under the practical temperature of diesel engine emissions.

It provides a design concept for the catalysts to improve the catalytic performance for soot combustion that the catalysts combine both advantages of the high contact efficiency by the structural effect of 3DOM supports with nanoporous walls and the abundant active oxygen species by the moderate interaction between supports and Pt nanoparticles. The materials consist of 3DOM supports with nanoporous walls and metal nanoparticle active sites may be useful for fundamental researches on the structural and metal–support synergistic effects and the potential practical applications in the catalytic oxidation of solid particles.

Acknowledgement

Appendix A. Supplementary data

Supplementary data associated with this article can be found, in the online version, at http://dx.doi.org/10.1016/j.apcatb.2013.03.019.

References

[1] J. Oi-Uchisawa, S. Wang, T. Nanba, A. Ohi, A. Obuchi, Applied Catalysis B 44 (2003) 207.
[2] A. Setiabudi, M. Makkee, J.A. Moulijn, Applied Catalysis B 42 (2003) 35.
[3] W.F. Shangguan, Y. Teraoka, S. Kagawa, Applied Catalysis B 16 (1998) 149.
[4] J. Liu, Z. Zhao, J. Wang, C. Xu, A. Duan, G. Jiang, Q. Yang, Applied Catalysis B 84 (2008) 185.
[5] J.O. Uchisawa, A. Obuchi, Z. Zhao, S. Kushiyama, Applied Catalysis B 18 (1998) 183.
[6] A. Setiabudi, B.A.A.L. van Setten, M. Makkee, J.A. Moulijn, Applied Catalysis B 35 (2002) 159.
[7] F.E. López-Suárez, A. Bueno-López, M.J. Illán-Gómez, Applied Catalysis B 84 (2008) 651.
[8] D. Reichert, T. Finke, N. Atanassova, H. Bockhorn, S. Kureti, Applied Catalysis B 84 (2008) 803.
[9] D. Fino, E. Cauda, D. Mescia, N. Russo, G. Saracco, V. Specchia, Catalysis Today 119 (2007) 257.
[10] M. Sun, L. Wang, B. Feng, Z. Zhang, G. Lu, Y. Guo, Catalysis Today 175 (2011) 100.
[11] J. Liu, Z. Zhao, C. Xu, A. Duan, Applied Catalysis B 78 (2008) 61.
[12] J.L. Hueso, A. Caballero, M. Ocaña, A.R. González-Elipe, Journal of Catalysis 257 (2008) 334.
[13] I. Atribak, A. Bueno-López, A. García-García, P. Navarro, D. Frías, M. Montes, Applied Catalysis B 93 (2010) 267.
[14] Z. Zhang, D. Han, S. Wei, Y. Zhang, Journal of Catalysis 276 (2010) 16.
[15] G. Mul, F. Kapteijn, C. Doornkamp, J.A. Moulijn, Journal of Catalysis 170 (1998) 258.
[16] M. Sadakane, T. Horiuchi, N. Kato, C. Takahashi, W. Ueda, Chemistry of Materials 19 (2007) 5779.
[17] Y. Liu, H. Dai, Y. Du, J. Deng, L. Zhang, Z. Zhao, C.T. Au, Journal of Catalysis 287 (2012) 149.

[18] G. Zhang, Z. Zhao, J. Xu, J. Zheng, J. Liu, G. Jiang, A. Duan, H. He, Applied Catalysis B 107 (2011) 302.
[19] J. Xu, J. Liu, Z. Zhao, J. Zheng, A. Duan, G. Jiang, Journal of Catalysis 282 (2011) 1.
[20] Y. Wei, J. Liu, Z. Zhao, A. Duan, G. Jiang, C. Xu, J. Gao, H. He, X. Wang, Energy & Environmental Science 4 (2011) 2959.
[21] H. Laversin, D. Courcot, E.A. Zhilinskaya, R. Cousin, A. Aboukaïs, Journal of Catalysis 241 (2006) 456.
[22] S. Carrettin, P. McMorn, P. Johnston, K. Griffin, C.J. Kiely, G.J. Hutchings, Physical Chemistry Chemical Physics 5 (2003) 1329.
[23] X. Zi, L. Liu, B. Xue, H. Dai, H. He, Catalysis Today 175 (2011) 223.
[24] Y. Zhai, D. Pierre, R. Si, W. Deng, P. Ferrin, A.U. Nilekar, G. Peng, J.A. Herron, D.C. Bell, H. Saltsburg, M. Mavrikakis, M. Flytzani-Stephanopoulos, Science 329 (2010) 1633.
[25] Z. Chen, Z. Guan, M. Li, Q. Yang, C. Li, Angewandte Chemie International Edition 50 (2011) 4913.
[26] Y. Wei, J. Liu, Z. Zhao, Y. Chen, C. Xu, A. Duan, G. Jiang, H. He, Angewandte Chemie International Edition 50 (2011) 2326.
[27] Y. Wei, J. Liu, Z. Zhao, A. Duan, G. Jiang, Journal of Catalysis 287 (2012) 13.
[28] K. Hinot, H. Burtscher, A.P. Weber, G. Kasper, Applied Catalysis B 71 (2007) 271.
[29] N. Tian, Z. Zhou, S. Sun, Y. Ding, Z.L. Wang, Science 316 (2007) 732.
[30] M. Sadakane, T. Horiuchi, N. Kato, K. Sasaki, W. Ueda, Journal of Solid State Chemistry 183 (2010) 1365–1371.
[31] B. Liu, Y. Liu, C. Li, W. Hua, P. Jing, Q. Wang, J. Zhang, Applied Catalysis B 127 (2012) 47–58.
[32] J. Liu, Z. Zhao, C. Xu, A. Duan, G. Jiang, Energy & Fuels 24 (2010) 3778.
[33] S. Li, J. Zheng, W. Yang, Y. Zhao, Materials Letters 61 (2007) 4784.
[34] W. Lin, A.A. Herzing, C.J. Kiely, I.E. Wachs, Journal of Physical Chemistry C 112 (2008) 5942.
[35] J.B. Park, J. Graciani, J. Evans, D. Stacchiola, S. Ma, P. Liu, A. Nambu, J.F. Sanz, J. Hrbek, J.A. Rodriguez, Proceedings of the National Academy of Sciences of the United States of America 106 (2009) 4975.
[36] G.N. Vayssilov, Y. Lykhach, A. Migani, T. Staudt, G.P. Petrova, N. Tsud, T. Skála, A. Bruix, F. Illas, V. Matolín, K.M. Neyman, J. Libuda, Nature Materials 10 (2011) 310.
[37] Z. Zhao, Y. Yamada, A. Ueda, H. Sakurai, T. Kobayashi, Catalysis Today 93–95 (2004) 163.
[38] R. Spinicci, A. Tofanari, Catalysis Today 8 (1990) 473.
[39] N. An, Q. Yu, G. Liu, S. Li, M. Jia, W. Zhang, Journal of Hazardous Materials 186 (2011) 1392.
[40] Y. Ji, Z. Zhao, A. Duan, G. Jiang, J. Liu, Journal of Physical Chemistry C 113 (2009) 7186.
[41] W.C. Conner, J.L. Falconer, Chemical Reviews 95 (1995) 759.
[42] W. Tang, Z. Hu, M. Wang, G.D. Stucky, H. Metiu, E.W. McFarland, Journal of Catalysis 273 (2010) 125.
[43] J. Guzman, B.C. Gates, Journal of the American Chemical Society 126 (2004) 2672.
[44] M. Hatanaka, N. Takahashi, T. Tanabe, Y. Nagai, K. Dohmae, Y. Aoki, T. Yoshida, H. Shinjoh, Applied Catalysis B 99 (2010) 336.
[45] J.P. Dacquin, M. Cabié, C.R. Henry, C. Lancelot, C. Dujardin, S.R. Raouf, P. Granger, Journal of Catalysis 270 (2010) 299.
[46] C. Ma, Z. Mu, J. Li, Y. Jin, J. Cheng, G. Lu, Z. Hao, S. Qiao, Journal of the American Chemical Society 132 (2010) 2608.
[47] Q. Fu, H. Saltsburg, M. Flytzani-Stephanopoulos, Science 301 (2003) 935.
[48] K. Leistner, A. Nicolle, P.D. Costa, Applied Catalysis B 111–112 (2012) 415.
[49] B. Bassou, N. Guilhaume, E.E. Iojoiu, D. Farrusseng, K. Lombaert, D. Bianchi, C. Mirodatos, Catalysis Today 159 (2011) 138.
[50] Y. Wei, J. Liu, Z. Zhao, C. Xu, A. Duan, G. Jiang, Applied Catalysis A 453 (2013) 250.
[51] P. Fornasiero, J. Kaspar, M. Graziani, Journal of Catalysis 279 (2011) 287.
[52] I. Atribak, F.E. López-Suárez, A. Bueno-López, A. García-García, Catalysis Today 176 (2011) 404.